In situ decoration of laser-scribed graphene with TiO2 nanoparticles for scalable high-performance micro-supercapacitors

In situ decoration of laser-scribed graphene with TiO_2 nanoparticles for scalable high-performance micro-supercapacitors

Laura Fornasini[a], Silvio Scaravonati[a], Giacomo Magnani[a], Alberto Morenghi[a], Michele Sidoli[a], Danilo Bersani[b], Giovanni Bertoni[c,d], Lucrezia Aversa[e], Roberto Verucchi[e], Mauro Riccò[a], Pier Paolo Lottici[b], Daniele Pontiroli[a,]*

a- Nanocarbon Laboratory, Department of Mathematical, Physical and Computer Sciences, University of Parma, Parco Area delle Scienze 7/A, 43124, Parma, Italy

b- Department of Mathematical, Physical and Computer Sciences, University of Parma, Parco Area delle Scienze 7/A, 43124 Parma, Italy

c- CNR – Istituto Nanoscienze, Via Campi 213/A, 41125, Modena, Italy

d- IMEM – CNR, Institute of Materials for Electronics and Magnetism, Parco Area delle Scienze 37/A, 43124, Parma, Italy

e- IMEM – CNR Institute of Materials for Electronics and Magnetism, Via alla Cascata 56/C - 38123 Povo – Trento, Italy

[*] Corresponding author. Tel. +39 0521 905236. E-mail: daniele.pontiroli@unipr.it (Daniele Pontiroli)

ABSTRACT

Graphene-based miniaturized supercapacitors, obtained via laser conversion of suitable precursors, have been attracting recent attention for the production of energy storage small-scale devices. In this work, a one-pot synthesis of TiO_2 nanoparticles embedded in porous graphene-based electrodes has been obtained with the LightScribe® technology, by converting the precursor materials through the absorption of a DVD burner infrared laser light. Enhanced electrochemical performance of devices has been achieved thanks to the combination of faradic surface reactions, arising from metal oxide nanoparticles, with the conventional electrochemical double layer capacitance, arising from porous graphene. Micro-supercapacitors, consisting of TiO_2-graphene electrodes, have been tested by investigating two hydrogel polymer electrolytes, based on polyvinyl alcohol/H_3PO_4 and polyvinyl alcohol/H_2SO_4, respectively. Specific areal capacitance up to 9.9 mF/cm^2 are obtained in TiO_2-graphene devices, corresponding to a volumetric capacitance of 13 F/cm^3 and doubling the pristine graphene-based device results. The micro-supercapacitors achieved specific areal energy and specific areal power of 0.22 μWh/cm^2 and 39 μW/cm^2, along with a cyclability greater than 3000 cycles. These high-performance results suggest laser-scribed TiO_2-graphene nanostructures as remarkable candidates in micro-supercapacitors for environment-friendly, large-scale and low-cost applications.

KEYWORDS

graphene, TiO_2, micro-supercapacitors, hydrogel polymer electrolyte, LightScribe® technology

1. INTRODUCTION

The increasing demand of micro power sources and small-scale energy storage devices has recently moved the attention to miniaturization. Micro power modules are required in devices such as sensors, portable and wearable electronics, radio frequency identification (RFID), or biomedical implants. These systems need self-powered wireless devices, which can work independently of an external power source. Supercapacitors (also called electrochemical double layer capacitors, EDLCs) can satisfy this requirement, thanks to their high specific power and their up to millions long life cycles [1–4].

In particular, the recent interest has been focused on miniaturized supercapacitors, also called micro-supercapacitors (MSCs), employed as power sources or energy storage harvesting units in microelectronic devices. Their total footprint area is in the range of square millimetre/centimetre, while their electrochemical performance in terms of energy and power densities is in the micro-scale. The first architecture of MSCs consists of a sandwich configuration, with film electrodes (less than 10 μm thick) facing each other and a solid electrolyte placed between them. However, in order to increase energy and power densities, a planar interdigitated arrangement is preferred, consisting of micro-electrodes in an in-plane configuration, instead of a vertical stack. The distance between the electrodes can be controlled and reduced, reaching small ion diffusion pathway from the electrolyte to the electrode; in addition, the increased accessibility of the electrodes sides ensures the use of their entire surface [1,5,6]. Gel electrolytes are usually used in interdigitated MSCs to reduce the electrolyte leakage and achieve better packaging of the devices [5,7,8].

As in conventional supercapacitors, essential features of the electrodes are high specific surface area with a hierarchical pore structure and good electrical conductivity [4,9–12]. Meeting these requirements, graphene-based systems, containing mono- or few-layers of

carbon atoms arranged in a honeycomb lattice, are currently explored as electrode materials in MSCs [12–14]. Furthermore, combining graphene with electroactive species is a promising attempt to enhance the electrochemical performance of supercapacitors, by introducing faradic surface effects in the storage mechanism, in addition to the electrostatic charge accumulation [15–18]. Transition metal oxides or hydroxides, such as manganese oxides [19], iron oxides [20], nickel oxides or hydroxides [21] and titanium dioxide [22] are currently explored, due to their multiple oxidation states, which can introduce redox contributions in the storage mechanism. The combination of these materials with graphene ensure a good electrical conductivity in the electrode.

Impressive results have been recently achieved in producing interdigitated graphene-based micro-electrodes using the laser light, through cost-effective techniques [23,24]. Carbonaceous precursor materials (such as graphite and graphene oxides) [25–29] or commercial polymers (such as polyimide and poly(ether ether ketone)) [25,30–34] are converted into electroactive materials by means of laser photoreduction. Different laser sources have been already examined, in continuous and pulsed mode, from the UV to the infrared range, to induce photothermal and/or photochemical reduction of carbon-based precursors into conductive graphene-based materials [25–35]. Graphite oxide (GO) can be easily converted into porous graphene-based products, thanks to the removal of oxygen containing groups, changing the electrical properties of the material from insulating to conductive. Infrared lasers of DVD burner drives, using the LightScribe® technology, are currently encouraged, since the production of hundreds of interdigitated electrodes can be achieved in less than one hour [27,36,37]. The technique has been recently explored to realize graphene-based electrodes with a straightforward process, starting from graphite oxide aqueous dispersion, realizing low-cost MSCs with remarkable electrochemical properties [27]. Furthermore, the performance of these devices can be improved by combining faradic

systems with graphene-based materials. Redox effects are obtained from iron oxide, cobalt oxide, molybdenum oxide [17], molybdenum disulfide [38] or titanium dioxide nanoparticles [39]. Among them, titanium dioxide (TiO_2), besides providing faradic effects, is considered a promising source to produce composite materials with graphene, thanks to its high thermal and chemical stability, low cost and low toxicity [22,39–44].

This work exploited a novel graphene-based composite material obtained by LightScribe® technique, with the simultaneous synthesis of TiO_2 nanoparticles (NPs) decorating the porous defective graphene structure. The LightScribe® writing process both converts suitable precursors into the active material and directly prints the electrodes ready for assembling the electrochemical device. This novel one-pot synthesis route demonstrated to be particularly effective to disperse TiO_2 NPs at the nanoscale, anchoring them to the graphene defects. To the best of our knowledge, a similar approach has not been investigated yet so far. In fact, several different techniques have been used to produce TiO_2-graphene composite materials, such as sol-gel method, solvothermal reactions or microwave-assisted routes. However, the synthesis of the combined materials often requires a multi-steps process, which first consists in graphene production, followed by the decoration with NPs. In some cases, the materials are only physically mixed, leading to phase segregation and NPs agglomeration, rather than promoting a combined material [22,39,41–44]. Our obtained composite nanostructure is competitive as electrode material, as displays both faradic and physical electrochemical storage capacity, hence improving the electrochemical performance of the same pristine graphene material without TiO_2 NPs.

High-performance MSCs have been produced with interdigitated electrodes and hydrogel polymer electrolytes in a planar configuration. Interdigitated patterns have been achieved on a proper DVD coating, based on an aqueous dispersion containing GO and titanium(IV)

isopropoxide, thanks to the photothermal process induced by the absorption of the infrared laser light. The process gives rise to the conversion of precursors into an electroactive and conductive composite material. The combination of the porous Laser-Scribed Graphite Oxide (LSGO) structure with a widespread decoration of anatase TiO_2 NPs in the electrode materials resulted in enhanced electrochemical properties compared to pristine graphene-based devices. Two hydrogel polymers based on polyvinyl alcohol (PVA)/H_3PO_4 and polyvinyl alcohol (PVA)/H_2SO_4 have been compared, achieving high-performance with specific areal capacitance up to 9.9 and 6.8 mF/cm^2, respectively. TiO_2 NPs decorating LSGO structures (henceforth called TiO_2-LSGO) obtained with the LightScribe® technology can be encouraged as remarkable material in MSCs for large-scale and low-cost production.

2. MATERIALS AND METHODS

2.1 Production of laser-scribed micro-supercapacitors

MSCs have been obtained through the LightScribe® technique in an interdigitated planar configuration [27]. The one-pot formation of TiO_2 NPs onto LSGO patterns has been achieved by means of the infrared laser of a LightScribe® DVD burner to produce the electrodes.

Graphite oxide and titanium(IV) isopropoxide have been used as precursor materials to be converted by the laser irradiation. GO obtained with Hummers' method [45] has been employed, due to its good solubility in water. Water as solvent in the preparation of the laser-scribed disc has been preferred to toxic, high-boiling temperature, organic solvents, typically employed to suspend graphene. An aqueous dispersion (2 mg/ml) of GO (GO-V50, Standard Graphene) has been sonicated for 8 h (30 min rest every 30 min of sonication to avoid

136 heating effects). Then, titanium(IV) isopropoxide (TTIP, 97%, Sigma-Aldrich Co.) has been
137 added in a TTIP:GO weight ratio 1.2:1, to obtain a final TiO_2:C molar ratio 1:8
138 (corresponding to a mass ratio of 0.8:1) [46]. The dispersion has been further sonicated for 30
139 min and stirred for 3 h, under Ar atmosphere. In order to decrease the TTIP hydrolysis
140 reaction rate, the pH of the dispersion has been controlled to neutrality. The laser-scribed disc
141 has been prepared by drop-casting 5 ml of the dispersion on a polyethylene terephthalate
142 (PET) disc (0.1 mm thick) and let it dry overnight under N_2 atmosphere, forming a film ~10
143 μm thick. The TTIP-GO-coated PET disc, glued to the surface of a LightScribe® DVD disc,
144 has been subjected to the LightScribe® process by the DVD burner infrared laser (λ=788 nm).
145 Interdigitated patterns are obtained using the LightScribe® *Nero CoverDesigner* software with
146 a typical writing time of about 20 min and 3 repetitions of the laser-scribing process, to fully
147 convert the precursors into TiO_2 NPs and LSGO [47]. Both electrodes of MSCs consist of
148 TiO_2-LSGO patterns, while unconverted parts between them prevent electrical contact of the
149 electrodes. Cu strips glued to the electrodes using silver paint were used as current collectors
150 in the device. The borders of the interdigitated area have been covered with Teflon® tape, to
151 separate the contacts from the electrolyte. Two hydrogel polymer electrolytes, consisting of
152 an aqueous solution of H_2O:acid:PVA (Sigma-Aldrich Co.) in the mass ratio 10:1:1, have
153 been tested, using H_3PO_4 and H_2SO_4 as acids, respectively [33]. The hydrogel polymer
154 electrolytes have been prepared starting from concentrated acid and deionized Milli-Q water,
155 which have been mixed with PVA powder under continuous stirring. The solution has been
156 heated to about 85 °C until it became clear. The gel-electrolyte has been drop-cast onto the
157 surface of the interdigitated area and let it dry overnight to eliminate water excess. To
158 investigate the effect of TiO_2 NPs on the devices, MSCs without TiO_2 have been prepared
159 following the same experimental procedure, using pristine GO aqueous dispersion.

2.2 Material characterization

The micro-structure of TiO_2-LSGO material has been examined by scanning transmission electron microscopy (STEM) and high-resolution imaging (HRTEM) using a field emission JEM-2200FS microscope (JEOL Ltd., Japan), equipped with a Schottky gun working at 200 kV (point resolution 0.19 nm), an in-column energy filter (Ω-type), a CCD high resolution camera, STEM detectors and an energy dispersive X-ray spectrometer (EDS). The material has been scratched from the interdigitated patterns of the laser-scribed surface obtained by the LightScribe® process, dispersed in isopropanol and deposited onto holey carbon films on copper grids. Simulation of the HRTEM image has been performed with the JEMS software [48], using Bloch waves dynamical calculation (50 reflections), quasi-parallel illumination (0.6 mrad) at 200 kV, 70 nm defocus, and a crystal thickness of 6 nm as inferred from the diameter of the titania nanoparticle in HRTEM. 1% of noise was added to better reproduce the noise in the experiment. Electron energy loss (EEL) spectra have been acquired on a Thermo Fischer Scientific Talos F200S in imaging mode (TEM) from a group of particles, to assure high signal to noise ratio due to the large collection angle. A Richardson–Lucy deconvolution with a low-loss spectrum has been done to reduce the contribution of multiple scattering and improve energy resolution, by following the indications in section 2.4 in [49].

Powder X-ray diffraction (PXRD) has been carried out on a small amount of TiO_2-LSGO material scratched from the PET substrate and sealed in a 0.5 mm diameter glass capillary. The measurement has been performed with a Bruker D8 Discover diffractometer, operating in Debye Scherrer geometry, equipped with copper anode (Cu-Kα) and a Rayonix MX225 2D area detector.

Micro-Raman spectroscopy has been performed with a Horiba LabRam micro-spectrometer (HORIBA Scientific, Kyoto, Japan), equipped with an Olympus microscope (Olympus,

Tokyo, Japan), using a 50x objective, in a backscattering geometry. The 473.1 nm line of a frequency-doubled Nd:YAG laser has been used as excitation, with a spectral resolution of ~2 cm^{-1}. To avoid heating effects, density filters have been used to reduce the laser power on the sample. The analysis has been performed on the TiO_2-LSGO material of the interdigitated patterns on the laser-scribed disc. Acquisitions have been recorded with typical exposure of 20-60 s, repeated 6 times for each measurement. The data analysis has been performed by the *LabSpec 5* built-in software.

X-Ray Photoelectron Spectroscopy (XPS) analysis has been carried out directly on the laser-scribed surface, which have been supported on a carbon tape (UHV compatible), using a UHV apparatus equipped with an X-ray source (Mg K_α photon at 1253.6 eV), while photoelectrons have been analyzed through a VSW HA100 hemispherical analyzer with a total energy resolution of 0.86 eV. Core level binding energies (BEs) have been normalized using as reference the Au 4f7/2 core level signal at 84.0 eV, acquired from a sputtered Au foil.

Electrical measurements have been performed on LSGO material on the laser-scribed surface. The electrical resistance has been measured by four-point probes method. The measurements have been carried out using a Keithley 6221 DC and AC current source and a Keithley 2182A Nanovoltmeter. The four probes consisted of aligned electrodes with golden tip.

The specific surface area (SSA) of LSGO material has been estimated by the physisorption of a common dye, methylene blue (MB), from the porous material, with UV-Visible spectrophotometry [37]. After a proper calibration to correlate the absorbance and the dye concentration, the amount of MB absorbed by LSGO has been evaluated. To perform the analysis, the material (~3 mg) has been removed from the laser-scribed surface obtained by the LightScribe® process, dispersed in a MB aqueous solution, whose initial concentration

was known, and stirred overnight. After centrifugation, the absorbance of the surnatant has been measured using a Jasco V-550 UV-Visible spectrophotometer to evaluate the variation of the MB concentration compared to the initial one.

2.3 Electrochemical characterization

The electrochemical performance of the electrodes and the devices have been tested with two- and three-electrode cell arrangement cyclic voltammetry (CV) at room temperature, respectively, with a Keithley Series 2400 Sourcemeter. In the three-electrode CV, the electrochemical characterization of the electrodes has been performed using either H_3PO_4 1 M or H_2SO_4 1 M aqueous electrolyte, an Ag/AgCl reference electrode and Pt counter electrode. The operating voltage range has been set between 0 and 1.0 V vs Ag/AgCl, applying a linear potential sweep with scan rates from 1 mV/s to 50 mV/s. The mean specific current ($<I>_s$) has been plotted as a function of the scan rate (ν), in order to highlight the faradic contribution in the presence of redox peaks. It is known that for a capacitive process the current is proportional to ν, while for faradic reactions it is proportional to $\nu^{1/2}$ [50,51].

Two electrode CV for the electrochemical characterization of the devices has been carried out using either PVA/H_3PO_4 and PVA/H_2SO_4 hydrogel electrolytes, applying a linear potential sweep with scan rates of 1, 5 and 10 mV/s. The optimal operating voltage window for cyclic voltammetry measurements has been identified between 0 and 0.8 V. Galvanostatic charge-discharge measurements (GCD) have been performed at room temperature, with a Landt CT2001A testing system by means of charge and discharge cycles at a fixed current, between 0 V and 0.8 V. Ten charge/discharge cycles have been tested at specific areal currents of 5, 10, 25, 50 and 100 $\mu A/cm^2$. Specific areal capacitance C_{SP} (mF/cm^2) of the material has been

calculated from the total capacitance C of the MSC, using the footprint area A_{AM} of the active material of both electrodes:

$$C_{SP} = 4\frac{C}{A_{AM}}$$

Specific areal energy E_{SP} ($\mu Wh/cm^2$) of the electrode material in the MSC has been evaluated by:

$$E_{SP} = \frac{CU_{max}^2}{2A_{AM}3600}$$

where U_{max} is the maximum region of electrochemical stability [52]. For each discharge cycle, the specific areal power P_{SP} has been obtained as the ratio between the specific areal energy (E_{SP}) and the total discharge time. The capacitance retention of the devices has been evaluated as the ratio of the specific areal capacitance at each cycle to the specific areal capacitance achieved in the first one, over at least 3000 cycles at 5 $\mu A/cm^2$. For each cycle, the Coulombic efficiency η_C is given by:

$$\eta_C = \frac{C_d}{C_c}$$

where C_d and C_c are the discharge and charge capacitance, respectively.

The energy efficiency η_E has been also calculated for each of the 3000 cycles at 5 $\mu A/cm^2$, given by the ratio between the energy during discharge and the energy during charge [53].

3. RESULTS

MSCs, either TiO_2-LSGO and LSGO, have been obtained by the LightScribe® technique in the planar configuration [27]. The scheme of the one-pot synthesis of TiO_2-LSGO and the

production of MSCs has been sketched in Figure 1 and the picture of a section of the laser-scribed disc is shown in the inset of Figure 1.

A detail of the micro-structure of the laser-scribed patterns is shown in the Supplementary Material in Figure S1.

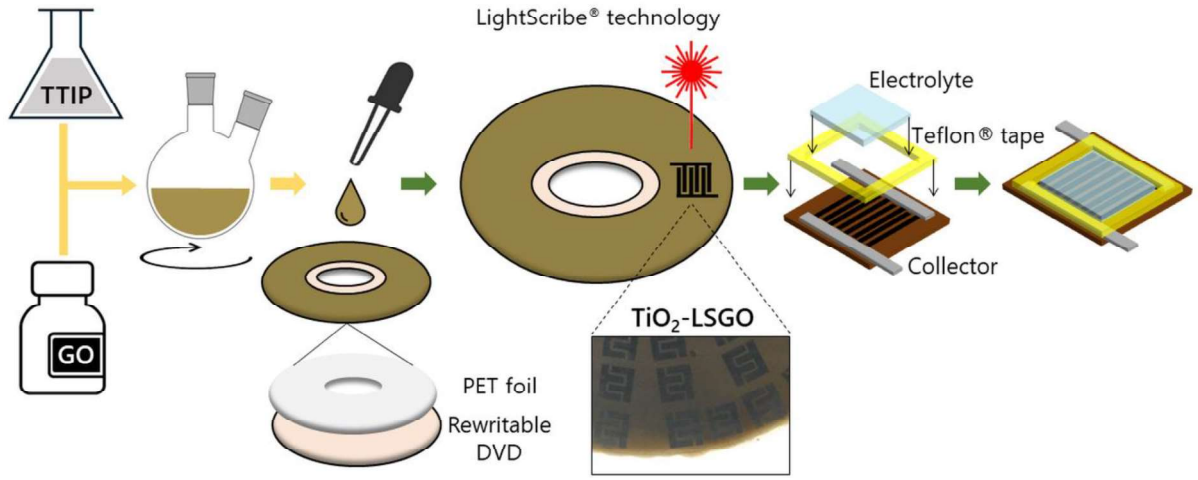

Figure 1. Scheme of the laser-scribed disc and MSCs production. The first steps (highlighted by yellow arrows) have been performed under inert atmosphere. *Inset:* image of the laser-scribed disc section.

In the process, the reactions of TTIP hydrolysis and condensation can be described by the equation:

$$Ti(OR)_m + (m-x)H_2O \rightarrow Ti(OH)_{m-x}(OR)_x + (m-x)R(OH)$$

where *R* is the $CH(CH_3)_2$ group, replaced with hydroxyl group during the hydrolysis reaction. Then, the hydroxyl groups condense with each other, eliminating water or isopropanol molecules.

During the laser photoreduction, a photothermal process occurred, as expected for infrared laser wavelengths [23,54]. The absorption of the infrared light can produce locally high temperatures (>10^3 °C), which promote TiO_2 crystallization. Besides, the temperature increase breaks the C-OOH and C=O bonds present in GO, which occur with gas release. The irradiated material results in a higher relative content of carbon compared to the precursor, due to the deoxygenation during the laser-scribing process. The conversion of GO into LSGO produce a porous material with a SSA of 180±20 m^2/g (Figure S2 in Supplementary Material), a value comparable with that observed for similar graphene-related materials [55]. LSGO material is also characterized by an increase in the electrical conductivity of five orders of magnitude to σ~1.1 S/cm (Table S1 in Supplementary Material).

277 **3.1 Electron Microscopy**

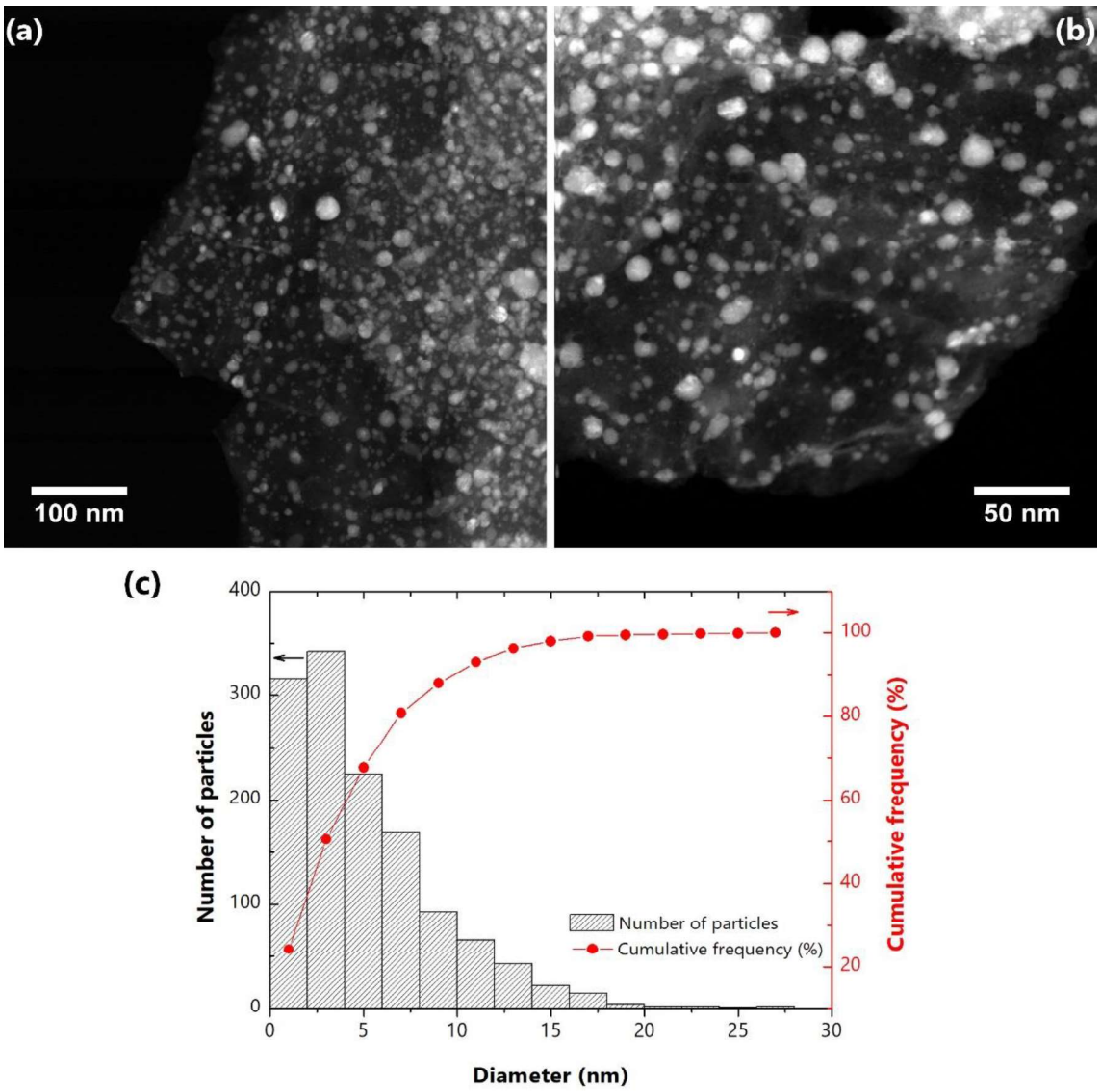

278

279 **Figure 2**. **(a)** and **(b)** STEM images of TiO_2-LSGO material collected at different magnification; **(c)**
280 TiO_2 diameter size distribution (in gray) and cumulative frequency curve (in red) of TiO_2-LSGO.

281

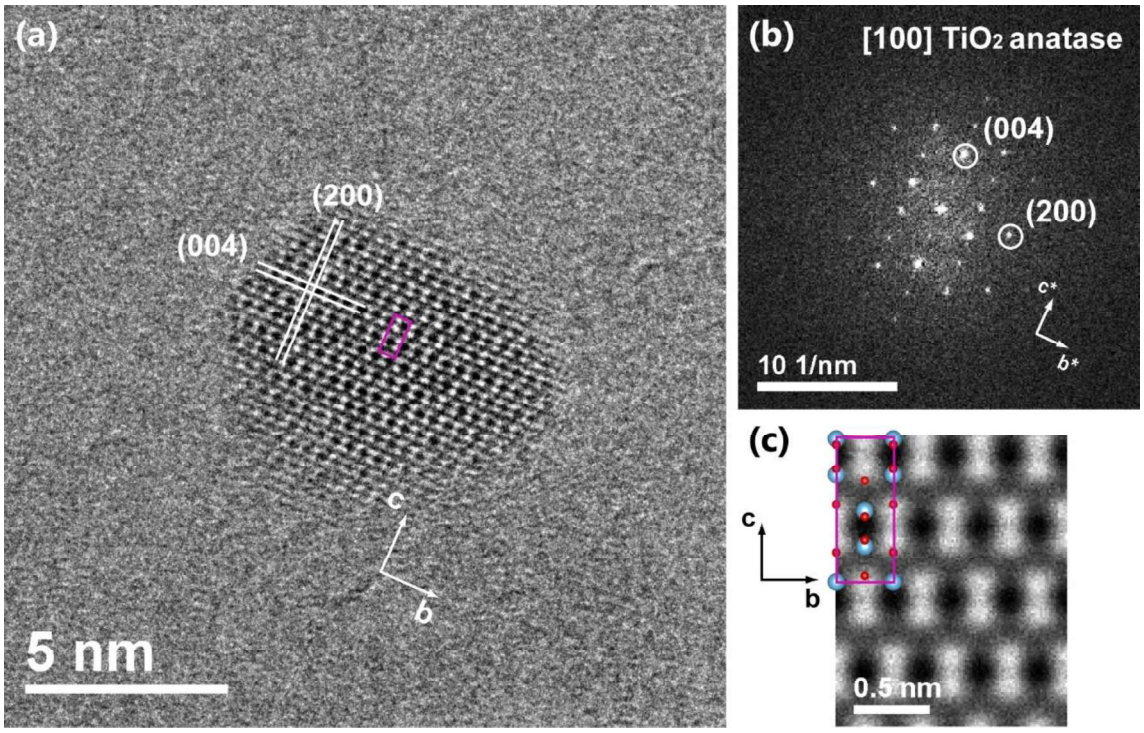

Figure 3. (a) HRTEM image of a TiO_2 nanoparticle of ~6 nm diameter; **(b)** FFT of the HRTEM image; **(c)**. Image simulation from TiO_2 anatase at 6 nm thickness. In the model, Ti atoms are light-blue and O atoms are red. The image contrast is in good agreement with the experiment, confirming the anatase (tetragonal) structure of the nanoparticle. The (200) and (004) planes are highlighted in (a) for clarity. The tetragonal cell is highlighted in purple in (a) and (c).

A widespread decoration of TiO_2-LSGO with TiO_2 NPs without agglomeration can be observed in the dark-field STEM image in Figure 2a and 2b, covering the whole graphene-based matrix (the NPs appear bright in the image, while the LSGO is darker). From a statistical analysis performed on about 1300 particles, the TiO_2 nanoparticle size distribution, while not entirely homogeneous, reveals that 90% of NPs diameter is under 10 nm, with an average of 3 nm (Figure 2c). Quasi-spherical shaped NPs are dominating, as shown in the HRTEM image of Figure 3a, and their structure is compatible with anatase TiO_2 (space group n.141, $I4_1/amd$), as revealed for instance by the presence of (200) and (004) reflections (Figure 3b) and confirmed by image simulation (Figure 3c). The EEL spectra from Ti-$L_{2,3}$ and O-K edges (reported in the Figure S3) agree with the spectra from nanostructured anatase

299 [56], in particular regarding the asymmetry of the e_g peak of the Ti-L_3 edge (rutile has the
300 opposite asymmetry of the e_g peak).

301 Anatase is confirmed as the main TiO_2 crystalline phase also by PXRD analysis, with its most
302 intense (101) reflection, occurring at $2\theta=25.3°$. PXRD results are shown in the
303 Supplementary Material (Figure S4).

304 The elemental composition of TiO_2-LSGO material performed by EDS analysis shows that
305 the Ti:C atomic ratio is 1:6, in good agreement with the expected molar ratio (TiO_2:C=1:8)
306 (Table S2).

307

308 **3.2 Raman spectroscopy**

309 The decoration of LSGO with TiO_2 anatase NPs is proved by the Raman analysis of TiO_2-
310 LSGO, as shown in Figure 4. The presence of anatase TiO_2 is confirmed by the main E_g
311 anatase vibrational mode in the Raman spectrum at ~155 cm^{-1}, expanded in the inset of
312 Figure 4. The peak is shifted and broadened compared to the crystalline anatase signal, as
313 expected for nanoparticle sizes under ~20 nm. According to the phonon confinement effect,
314 in the case of finite size crystals, the main anatase peak is a convolution of many
315 contributions, following the phonon dispersion curve, instead of a single sharp Lorentzian, as
316 for ideal crystalline anatase. The observed peak position at ~155 cm^{-1}, shifted from the 143
317 cm^{-1} of the crystalline reference, suggests the presence of ~5 nm size NPs, as predicted by the
318 phonon confinement model [57]. The one-pot formation of the TiO_2-LSGO combined
319 material is highlighted by the presence of the typical D and G bands of carbon-based
320 materials, along with the anatase feature (Figure 4). The G band, related to the E_{2g} phonon
321 mode of the sp^2 domains in graphitic materials, and the D band, arising from structural

defects in disordered samples, are observed at ~1370 cm^{-1} and ~1600 cm^{-1}, respectively [58]. The broadening of D and G band compared to ordered crystalline materials confirms the highly defective structure of LSGO [59].

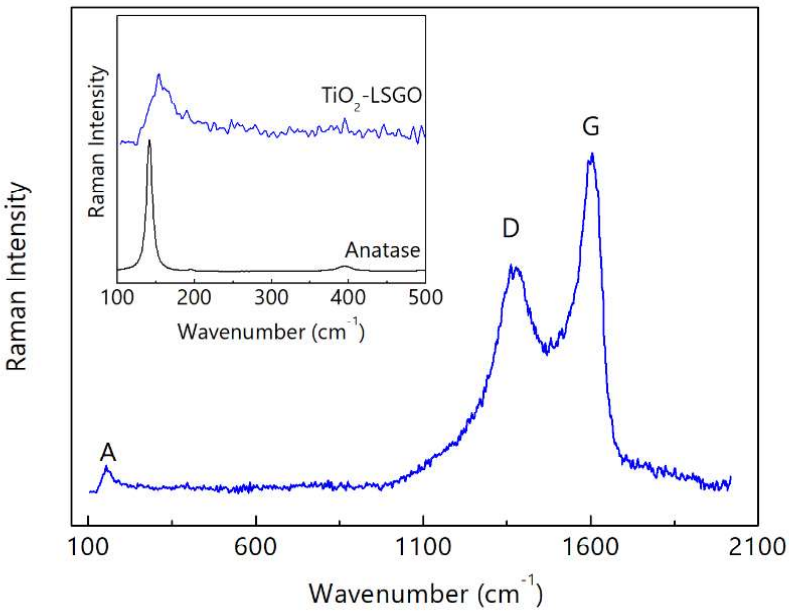

Figure 4. Raman spectrum of TiO_2-LSGO with the most intense anatase E_g vibrational mode (A) and characteristic graphene-based materials bands (D and G). *Inset:* the main anatase peak in TiO_2-LSGO spectrum (in blue) is expanded and compared with the reference crystalline anatase spectrum (in black).

3.3 X-ray Photoelectron Spectroscopy

XPS core level spectra of C1s and O1s for GO and LSGO samples are shown in Figure 5a and 5b. In GO main peaks are positioned at higher BE than expected, about +4 eV, due to charging phenomena already evidenced in samples of GO [26]. After laser treatment, this charge shift is no more detected and the peak positions are aligned to the expected standards [60]. In C1s core level (Figure 5a), we can assign the peak at 288.4 eV to the graphene emission (C=C-C bonds), while the other main feature at 290.8 eV is due to C-O bonds. Other peaks are present and related to C=O, COOH/COOR, defects in the graphene structure

and contaminants (Table S3). O1s core level (Figure 5b) shows the corresponding oxidized carbon species. The laser treatment completely changes the surface chemical properties, as shown in LSGO spectra. The C/O stoichiometry ratio increase from 2.3 to 15.2, suggesting a significant oxygen loss. In C1s core level, all oxygen related peaks decrease in intensity and the graphene main component at 284.4 eV is sharper (Table S3). O1s core level (Figure 5b) follows the same trend, with suppression of the O-C components and absence of charge shift.

XPS core level spectra of Ti2p and O1s core levels for GO and LSGO sample with TiO_2 nanoparticles are shown in Figure 5c and 5d. Charge shift is present for GO samples and suppressed for LSGO, in which the $Ti2p_{3/2}$ peak position is 459.2 eV compatible with Ti^{4+} oxidized species. Ti2p is a single, narrow peak (FWHM of $Ti2p_{3/2}$ is 1.6 eV in both spectra), characterized by the well-known $Ti_{3/2}$ and $Ti_{1/2}$ spin-orbit splitting, without any further contribution from low valence Ti species and the corresponding O1s contribution has a BE distance of (71.8±0.1) eV [61]. The O/Ti ratio is 2.0±0.05, thus indicating the presence of stoichiometric TiO_2 nanoparticles in both samples.

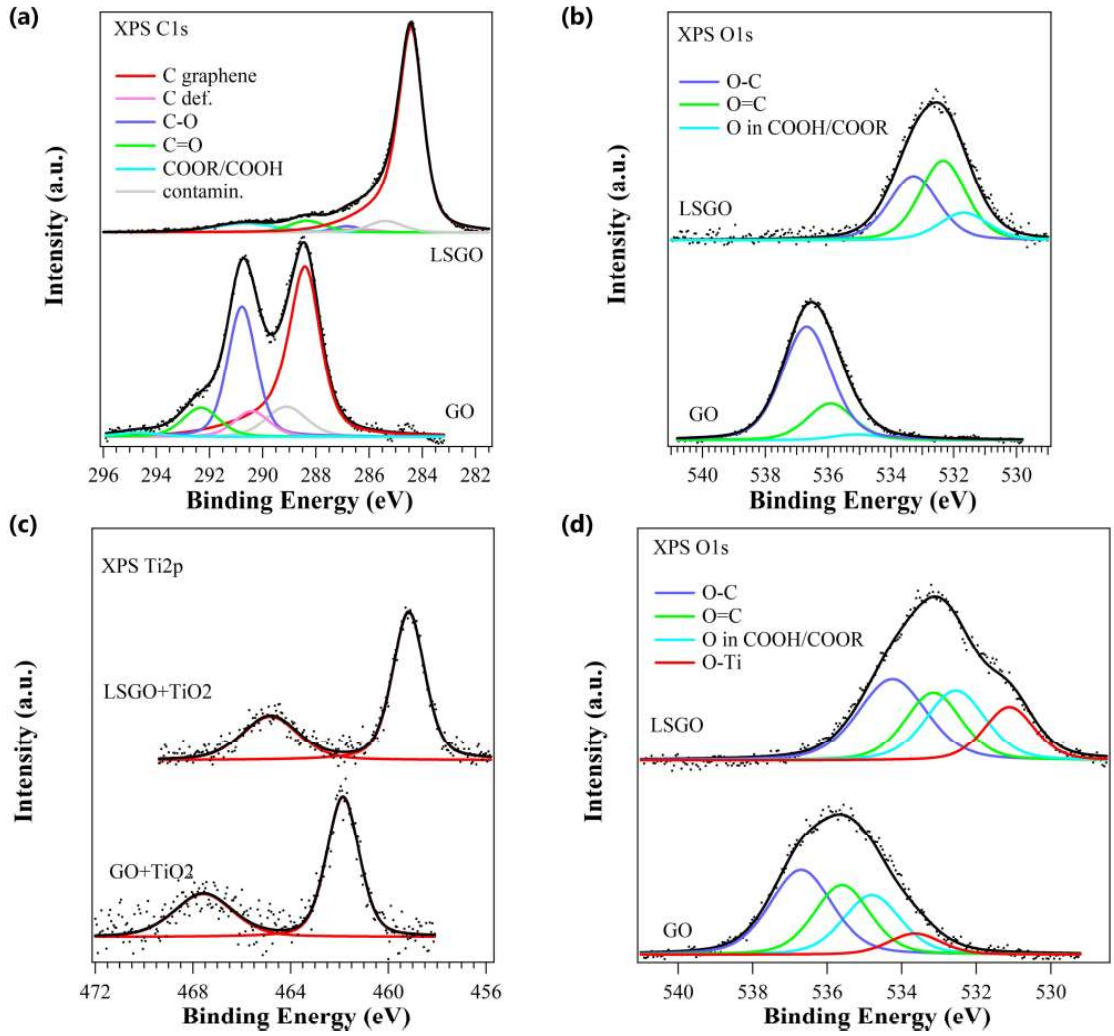

Figure 5. XPS spectra of **(a)** C1s and **(b)** O1s core levels of GO and LSGO; **(c)** Ti2p and **(d)** O1s core levels of GO and LSGO samples, with TiO_2 nanoparticles. All spectra are normalized to peak height and background subtracted.

The residual oxygen atoms bonded to carbon network after the laser treatment, as detected by XPS analysis, are expected to contribute to the lower value of conductivity of LSGO as compared to pure graphene. In addition, the presence of defects in LSGO, related to its wrinkled structure, as observed in STEM image in Figure 2a, contributes to limit the electrical conductivity. On the other hand, the defective structure of LSGO is beneficial for the growth of small sized TiO_2 nanoparticles. The simultaneous crystallization of TiO_2 NPs

and conversion of GO into LSGO have been promoted by the local increase in temperature, because of the absorption of laser radiation by graphite oxide.

3.4 TiO_2-LSGO and LSGO MSCs electrochemical performance

CV has been performed in a three-electrode cell arrangement to characterize LSGO and TiO_2-LSGO materials before assembling the devices. The results are shown in the Supplementary Material.

The electrochemical properties of the laser-scribed MSCs have been evaluated with two different hydrogel polymer electrolytes, namely PVA/H_3PO_4 and PVA/H_2SO_4. Since the best electrochemical performance has been obtained with the PVA/H_3PO_4-based electrolyte, these results will be discussed here, while those obtained with PVA/H_2SO_4-based electrolyte are reported in the Supplementary Material.

The electrochemical behaviour of the TiO_2-LSGO composite material consists of two contributions: the first one has a capacitive origin, typical of EDLCs and it is due to the electrostatic charge accumulation at the electrode-electrolyte interface on porous conductive electrodes, as expected for graphene-based materials. The second one arises from surface faradic processes and originates from the electron transfer, occurring during charge and discharge cycles with the redox-active TiO_2 NPs [62].

The results on MSCs with PVA/H_3PO_4 hydrogel polymer electrolyte are shown in Figures 6, 7 and 8. Both EDLC and faradic effects are observable in the CV curves of TiO_2-LSGO MSCs (Figure 6a). Faradic contribution has been confirmed by the three-electrode cell arrangement CV results, shown in the Supplementary Material (Figures S5 and S6) [51]. In contrast, LSGO MSCs show only the capacitive behaviour, with a nearly rectangular CV

388 curve (Figure 6b). When TiO_2 NPs are combined with LSGO (TiO_2-LSGO), an enlargement
389 in the area of CV curves and a slight deviation from the rectangular shape are observed. We
390 can exclude that this behaviour is due to an electronic leakage, possibly arising from the
391 unconverted GO regions. In that case, we would expect the same effect also in LSGO MSCs,
392 which has not been observed. Thus, the deviation from the rectangular shape can be ascribed
393 to a faradic effect. The enlargement of the area of CV curves in TiO_2-LSGO compared to
394 LSGO MSCs suggests an increase in specific areal capacitance, since at equal scan rate
395 (dV/dt) the specific areal capacitance is proportional to the integral area of the curve. In
396 particular, as depicted from the comparison at 1 mV/s in Figure 6c, redox processes seem to
397 occur at ~0.2 V in TiO_2-LSGO. The better performance at lower scan rates suggests that the
398 faradic contribution is characterized by a different process time scale compared to the EDLC
399 capacitance.

400 The combined behaviour of TiO_2-LSGO MSCs is also confirmed by galvanostatic charge and
401 discharge measurements, as shown in Figure 7. Triangular-shaped charge and discharge
402 curves are achieved by LSGO MSCs at different current densities (Figure 7b), suggesting a
403 purely electrostatic charge storage. A slight deviation from the ideal trend is obtained at the
404 lowest specific areal current (5 $\mu A/cm^2$), suggesting that also LSGO can give a contribution,
405 while small, to the faradic behaviour. Residual oxygen (not removed by the LightScribe®
406 process) in carbonyl functional groups reacts with H^+ of the electrolyte in acidic solutions
407 [62,63]. In TiO_2-LSGO MSCs, charge and discharge curves show a pronounced deviation
408 from the triangular shape (Figure 7a). Further contribution to the faradic system is attributed
409 to the presence of TiO_2 NPs.

410 Specific areal capacitance, as obtained from the slope of the galvanostatic curves (GCD) is
411 shown in Figure 8a, at each current density. In TiO_2-LSGO MSCs, the highest specific areal

412 capacitance amounts at 9.9 mF/cm^2 at a current density of 5 μA/cm^2, more than twice the
413 value for LSGO MSCs (4.6 mF/cm^2), at the same current density. These results prove a clear
414 increase of performance of these MSCs, compared to other laser-scribed graphene-based
415 devices (Table S4).

416 As current density is greater, the discrepancy in specific areal capacitance between the
417 devices is reduced, and comparable values are obtained at 50 μA/cm^2. Specific areal energy
418 achieved maximum values of 0.22 μWh/cm^2 in TiO_2-LSGO MSCs, at 5 μA/cm^2 (specific
419 areal energy values at each current density are reported in Figure S7). Specific areal energy
420 vs specific areal power is shown in a Ragone plot in Figure 8b. Higher specific areal energy
421 is generally achieved in TiO_2-LSGO devices, while specific areal power is comparable in
422 both LSGO and TiO_2-LSGO devices.

423 Remarkable cycling stability is achieved in TiO_2-LSGO MSCs. The capacitance retentions
424 over 3000 cycles are compared in Figure 8c. TiO_2-LSGO MSCs show an 81% retention of
425 the initial specific areal capacitance, showing a better overall trend than LSGO MSCs value
426 (72%). Fluctuations observed in the LSGO devices are related to the low current level, close
427 to the instrument sensitivity and more affected by noise. To compare TiO_2-LSGO and LSGO
428 MSCs with a comparable specific areal current, the current level for LSGO is lower due to
429 the smaller mass of the active material of the device. The mean Coulombic efficiency over
430 3000 cycles is >98% for both MSCs (Figure S8). The energy efficiency after 3000 cycle is
431 about 70% (Figure S8).

432

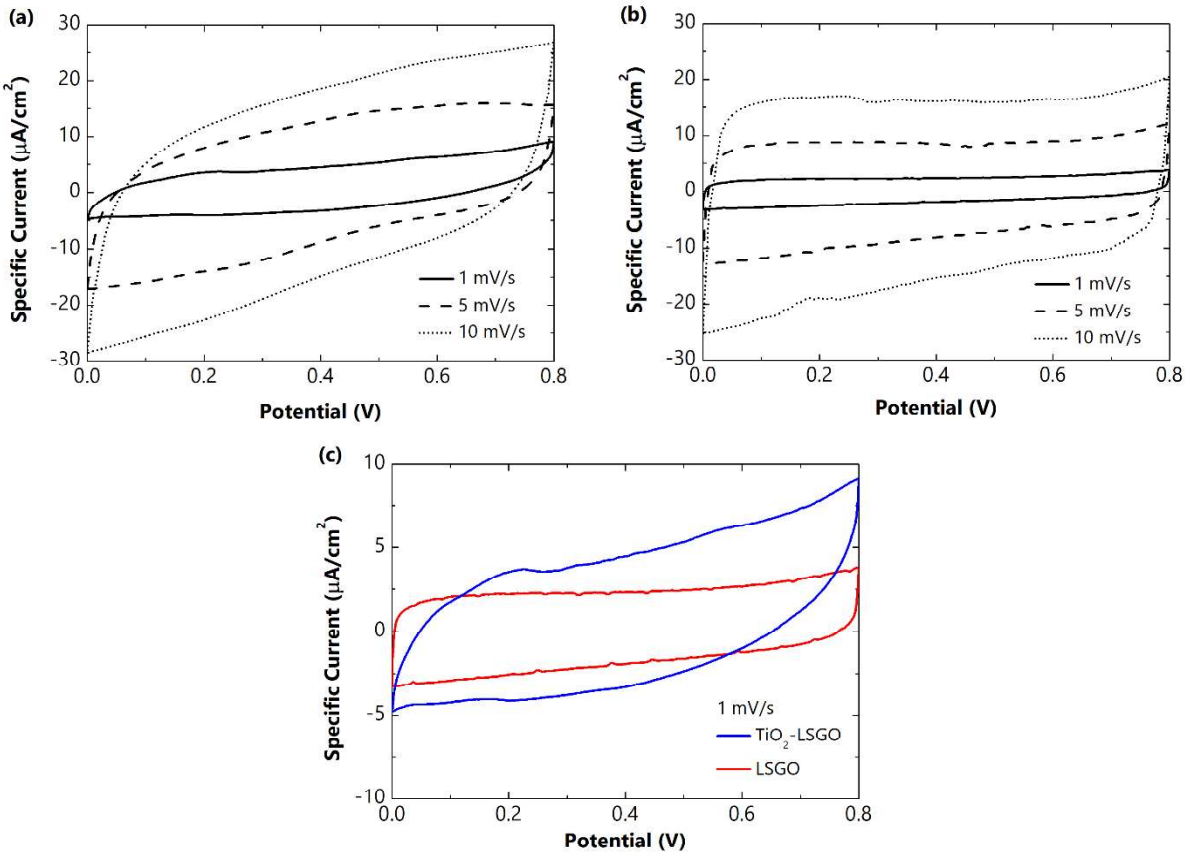

433

434 **Figure 6**. Cyclic voltammetry curves of laser-scribed MSCs with PVA/H_3PO_4 gel electrolyte: **(a)**
435 TiO_2-LSGO and **(b)** LSGO curves at different scan rates; **(c)** TiO_2-LSGO and LSGO curves at the rate
436 of 1 mV/s.

437

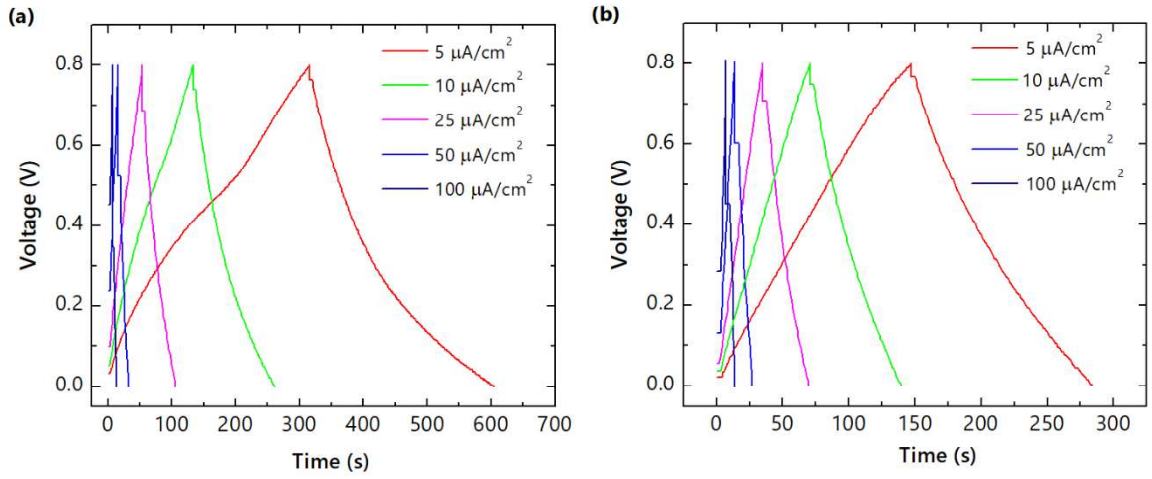

438

439 **Figure 7.** Galvanostatic charge and discharge curves at different specific areal currents of **(a)** TiO_2-
440 LSGO and **(b)** LSGO MSCs with PVA/H_3PO_4 gel electrolyte.

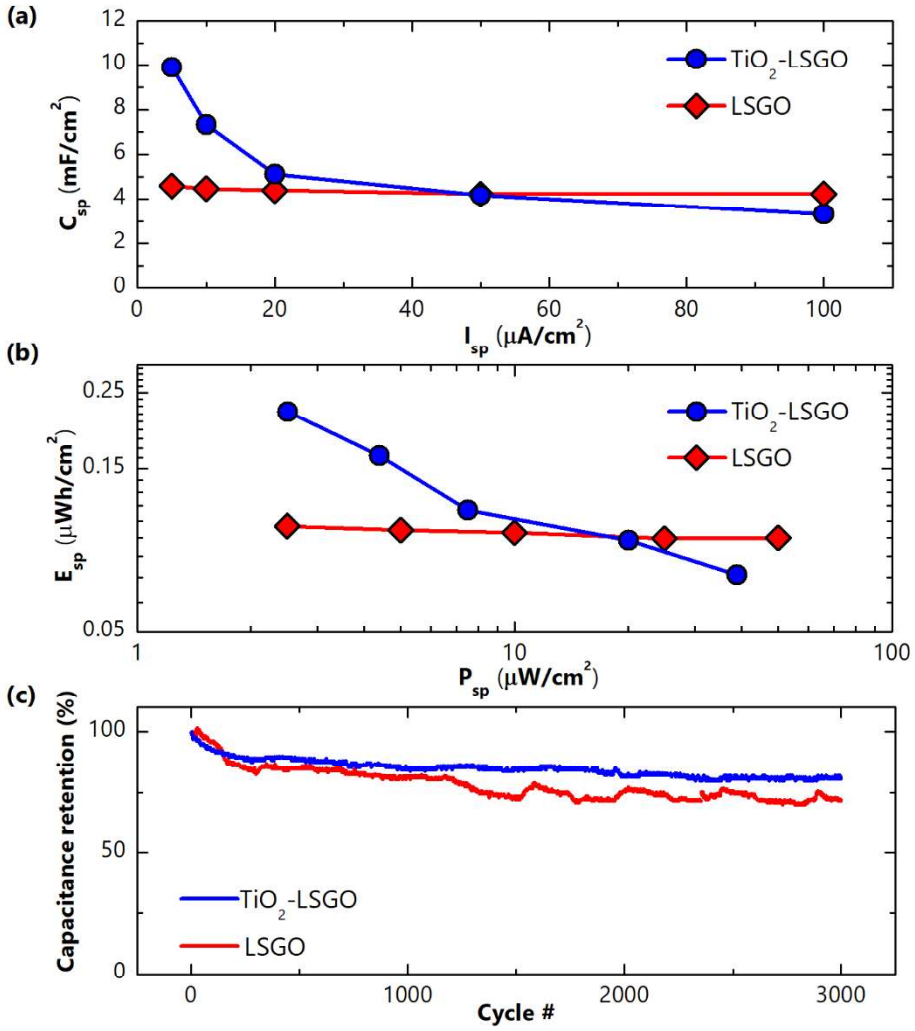

441

442 **Figure 8. (a)** Specific areal capacitance and **(b)** Ragone plot achieved for TiO_2-LSGO and LSGO
443 MSCs with PVA/H_3PO_4 gel electrolyte at different specific areal currents. Values are averaged on 10
444 cycles at each specific areal current. **(c)** Capacitance retention over 3000 charge and discharge cycles
445 at 5 μA/cm^2.

446

447 The results on MSCs with PVA/H_2SO_4 hydrogel polymer electrolyte are discussed in the
448 Supplementary Material and shown in Figures S9-S14. Similar electrochemical behaviour has
449 been observed in the MSCs, as for the PVA/H_3PO_4 hydrogel electrolyte. The increase in the
450 performance has been confirmed for TiO_2-LSGO MSCs, compared to LSGO MSCs (highest
451 specific areal capacitance amounting at 6.8 mF/cm^2 and 5.6 mF/cm^2 at a current density of 5
452 μA/cm^2 for TiO_2-LSGO and LSGO, respectively). A remarkable cycling stability has been
453 achieved also in PVA/H_2SO_4 devices (capacitance retention >80% after 3000 cycles).

4. DISCUSSION

The electrochemical results on TiO_2-LSGO and LSGO MSCs show an increase in the performance in the presence of anatase TiO_2 nanoparticles in the electrodes, compared to the LSGO devices. The enhancement is achieved for both the hydrogel polymer electrolytes tested, based on PVA/H_3PO_4 and PVA/H_2SO_4.

In LSGO devices, a typical EDLC behaviour is observed, both from the rectangular shape of CV curves and from the linear voltage dependence on time in the GCD curves. In TiO_2-LSGO devices, both capacitive and pseudocapacitive effects are achieved. Anatase nanoparticles are expected to introduce redox contributions in the charge storage mechanism [41,42]. This effect is here confirmed both in the cyclic voltammetry curves and from the galvanostatic charge and discharge measurements. In CV curves, the integral area is enlarged in TiO_2-LSGO. In addition, at low scan rates (Figure 6c), redox peaks contributing to the increase in specific areal capacitance are also observed in MSCs with both the electrolytes. Regarding GCD investigation, the higher specific areal capacitance is confirmed by the slope of galvanostatic curves. Specific areal energy is higher than that in LSGO devices, especially at low current density, as observed for the specific areal capacitance. Remarkably, the TiO_2-LSGO devices exhibit excellent cycling stability in retaining the specific areal capacitance for more than 3000 cycles.

TiO_2 in anatase phase has been reported to lead to a higher increase in capacitance compared to the other TiO_2 polymorphs, i.e. rutile, which is instead considered as a better source of cycle stability in supercapacitors [41]. Here, as TiO_2 nanoparticles consist of anatase, a good specific areal capacitance is proved and a great stability is additionally achieved.

Regarding the hydrogel polymer electrolytes, good performance has been observed with two different electrolytes, confirming the appropriate use of electrolytes based on acidic

478 conductive substances. It has been proved that a quick diffusion of H^+ from the electrolytes
479 (here, from H_3PO_4 and H_2SO_4 solutions) can easily occur into graphene-based electrodes
480 pores [5]. Comparing the gel electrolytes, the PVA/H_3PO_4-based TiO_2-LSGO micro-
481 supercapacitors give rise to an overall higher improvement in the electrochemical
482 performance than PVA/H_2SO_4-based TiO_2-LSGO devices.

483 It is well known that transition metal oxides, such as TiO_2, can introduce redox effects in the
484 charge storage mechanism, achieving a higher amount of charge stored in supercapacitors.
485 The EDLC-like behaviour can be combined to the redox contribution [22,41,64,65]. In TiO_2,
486 the contribution to the charge storage can be ascribed to two synergic mechanisms. The first
487 consists of the intercalation and de-intercalation of cations from the electrolyte (H^+ in the
488 electrolytes tested here) into the electrode, occurring during the charge and the discharge of
489 the supercapacitor, while the second one involves surface adsorption, according to [41]:

490 $$(TiO_2)_{surface} + H_3O^+ + e^- \leftrightarrow (TiO_2^- H_3O^+)_{surface}$$

491 Both mechanisms are reported to determine the change in the oxidation state of Ti, from Ti^{4+}
492 to Ti^{3+} with reduction and oxidation reactions, as confirmed from redox peaks in cyclic
493 voltammetry curves in three-electrode cell arrangement (Figures S5 and S9). This process is
494 likely to occur only in one of the two electrodes of the MSC, typically the negatively
495 polarised one (the behaviour of the other electrode is assumed to be purely capacitive), and
496 should not depend on the electrolyte used, as far as acidic electrolytes are concerned.

497 The higher performance achieved with the PVA/H_3PO_4-based electrolyte can be ascribed to
498 the larger amount of available H^+ ions than in PVA/H_2SO_4-based one, keeping the same
499 concentration [66]. In addition, the solvated ionic radius of $(PO_4)^{3-}$ is slightly smaller than
500 that of $(SO_4)^{2-}$, facilitating its insertion in the porous cavities of LSGO [67]. Furthermore,

501 ionic conductivity of H_3PO_4 aqueous electrolyte is higher than that of H_2SO_4 one, being
502 beneficial for the device performance [68]. The synergistic effect of these factors is expected
503 to contribute to a higher electrochemical performance in PVA/H_3PO_4-based MSCs. Overall,
504 the results on TiO_2-LSGO combined material, consisting of a widespread distribution of
505 anatase TiO_2 nanoparticles over graphene-based material, show competitive properties
506 compared to other graphene-based electrodes (Table S4, Figures S15 and S16) and
507 demonstrate the remarkable electrochemical performance of the MSCs.

508

509 ## 5. CONCLUSION

510 In summary, the production of the TiO_2-LSGO combined material has been successfully
511 achieved through the one-pot synthesis of TiO_2 anatase nanoparticles onto Laser-Scribed
512 Graphite Oxide by the LightScribe® technique, using a low-cost and scalable method. The
513 local increase in temperature as a result of the absorption of the DVD burner infrared laser
514 radiation by GO promotes both the nanoparticles crystallization and the conversion of GO
515 into graphene-based material. An extensive spread of anatase NPs has been obtained onto the
516 porous LSGO surface.

517 The TiO_2-LSGO combined material, arranged into interdigitated patterns obtained by the
518 LightScribe® process, has been used as electrode material of planar MSCs, which have been
519 tested with two hydrogel polymer electrolytes, based on PVA/H_3PO_4 and PVA/H_2SO_4,
520 respectively. Nanocrystalline TiO_2 combined with LSGO gives rise to a considerable increase
521 in the electrochemical performance, compared to the pristine LSGO. The enhanced results
522 obtained with the TiO_2-LSGO MSCs have been ascribed to the combined behaviour of the
523 electrode material, including faradic effects due to redox contributions (arising from TiO_2
524 NPs) and capacitive storage mechanisms (arising from LSGO). Specific areal capacitance up

to 9.9 and 6.8 mF/cm^2 has been achieved in TiO_2-LSGO MSCs with PVA/H_3PO_4 and PVA/H_2SO_4 polymer hydrogel electrolytes, respectively. Improvement in the specific areal energy has also been obtained in TiO_2-LSGO MSCs (0.22 μWh/cm^2 and of 0.15 μWh/cm^2 for the two electrolytes, respectively). Cycling stability has been maintained for thousands of cycles.

The impressive electrochemical performance of TiO_2-LSGO devices reveals that the one-pot formation of TiO_2 nanoparticles onto laser-scribed graphene structures by the LightScribe® technique can be a successful strategy to produce cost-effective, low-toxicity and large-scale micro-supercapacitors with competitive electrochemical performance for energy storage.

CREDIT AUTHORSHIP CONTRIBUTION STATEMENT

Laura Fornasini: writing – original draft, validation, formal analysis, investigation, visualization, **Silvio Scaravonati:** validation, formal analysis, investigation, visualization, **Giacomo Magnani:** validation, investigation, **Alberto Morenghi:** investigation, **Michele Sidoli:** investigation, **Danilo Bersani:** conceptualization, supervision, **Giovanni Bertoni:** investigation, formal analysis, **Lucrezia Aversa:** investigation, formal analysis, **Roberto Verucchi:** investigation, formal analysis, **Mauro Riccò:** conceptualization, **Pier Paolo Lottici:** visualization, **Daniele Pontiroli:** conceptualization, methodology, writing – original draft, visualization, supervision, project administration.

DECLARATION OF COMPETING INTEREST

The authors declare that they have no known competing financial interests or personal relationships that could have appeared to influence the work reported in this paper.

APPENDIX A. SUPPLEMENTARY MATERIAL

Supplementary Material includes micro-structure of the laser-scribed material; specific surface area of LSGO; electrical resistance and conductivity of GO and LSGO; EEL spectroscopy; EDS analysis; powder X-ray diffraction; XPS lineshape analysis on GO and LSGO; comparison among different micro-supercapacitors with laser-scribed graphene-based electrodes; supplementary electrochemical results of TiO_2-LSGO and LSGO MSCs with PVA/H_3PO_4-based electrolyte; three-electrode cell cyclic voltammetry; electrochemical results of TiO_2-LSGO and LSGO MSCs with PVA/H_2SO_4-based electrolyte; Ragone plot comparison among this work MSCs and other graphene-based energy storage devices.

560 REFERENCES

561

562 [1] M. Beidaghi, Y. Gogotsi, Capacitive energy storage in micro-scale devices: Recent
563 advances in design and fabrication of micro-supercapacitors, Energy Environ. Sci. 7
564 (2014) 867–884. https://doi.org/10.1039/c3ee43526a.

565 [2] Z.L. Wang, Toward self-powered sensor networks, Nano Today. 5 (2010) 512–514.
566 https://doi.org/10.1016/j.nantod.2010.09.001.

567 [3] P. Simon, Y. Gogotsi, Materials for electrochemical capacitors, Nat. Mater. 7 (2008)
568 845–854. https://doi.org/10.1038/nmat2297.

569 [4] P. Simon, Y. Gogotsi, Charge storage mechanism in nanoporous carbons and its
570 consequence for electrical double layer capacitors, Philos. Trans. R. Soc. A Math.
571 Phys. Eng. Sci. 368 (2010) 3457–3467. https://doi.org/10.1098/rsta.2010.0109.

572 [5] J.J. Yoo, K. Balakrishnan, J. Huang, V. Meunier, B.G. Sumpter, A. Srivastava, M.
573 Conway, A.L. Mohana Reddy, J. Yu, R. Vajtai, P.M. Ajayan, Ultrathin planar
574 graphene supercapacitors, Nano Lett. 11 (2011) 1423–1427.
575 https://doi.org/10.1021/nl200225j.

576 [6] Z.S. Wu, K. Parvez, X. Feng, K. Müllen, Graphene-based in-plane micro-
577 supercapacitors with high power and energy densities, Nat. Commun. 4 (2013) 1–8.
578 https://doi.org/10.1038/ncomms3487.

579 [7] Z. Niu, L. Zhang, L. Liu, B. Zhu, H. Dong, X. Chen, All-solid-state flexible ultrathin
580 micro-supercapacitors based on graphene, Adv. Mater. 25 (2013) 4035–4042.
581 https://doi.org/10.1002/adma.201301332.

582 [8] C. Zhong, Y. Deng, W. Hu, J. Qiao, L. Zhang, J. Zhang, A review of electrolyte
583 materials and compositions for electrochemical supercapacitors, Chem. Soc. Rev. 44
584 (2015) 7484–7539. https://doi.org/10.1039/c5cs00303b.

585 [9] D. Pontiroli, S. Scaravonati, G. Magnani, L. Fornasini, D. Bersani, G. Bertoni, C.
586 Milanese, A. Girella, F. Ridi, R. Verucchi, L. Mantovani, A. Malcevschi, M. Riccò,
587 Super-activated biochar from poultry litter for high-performance supercapacitors,
588 Microporous Mesoporous Mater. 285 (2019) 161–169.
589 https://doi.org/10.1016/j.micromeso.2019.05.002.

590 [10] J. Gamby, P.L. Taberna, P. Simon, J.F. Fauvarque, M. Chesneau, Studies and
591 characterisations of various activated carbons used for carbon/carbon supercapacitors,
592 J. Power Sources. 101 (2001) 109–116. https://doi.org/10.1016/S0378-7753(01)00707-
593 8.

594 [11] G. Moreno-Fernández, J.L. Gómez-Urbano, M. Enterría, T. Rojo, D. Carriazo, Flat-
595 shaped carbon-graphene microcomposites as electrodes for high energy
596 supercapacitors, J. Mater. Chem. A. 7 (2019) 14646–14655.
597 https://doi.org/10.1039/c9ta03295a.

598 [12] A. González, E. Goikolea, J.A. Barrena, R. Mysyk, Review on supercapacitors:

599 Technologies and materials, Renew. Sustain. Energy Rev. 58 (2016) 1189–1206.
600 https://doi.org/10.1016/j.rser.2015.12.249.

601 [13] R. Raccichini, A. Varzi, S. Passerini, B. Scrosati, The role of graphene for
602 electrochemical energy storage, Nat. Mater. 14 (2015) 271–279.
603 https://doi.org/10.1038/nmat4170.

604 [14] M. Pumera, Graphene-based nanomaterials for energy storage, Energy Environ. Sci. 4
605 (2011) 668–674. https://doi.org/10.1039/c0ee00295j.

606 [15] A. Afif, S.M. Rahman, A. Tasfiah Azad, J. Zaini, M.A. Islan, A.K. Azad, Advanced
607 materials and technologies for hybrid supercapacitors for energy storage – A review, J.
608 Energy Storage. 25 (2019) 100852. https://doi.org/10.1016/j.est.2019.100852.

609 [16] V. Augustyn, P. Simon, B. Dunn, Pseudocapacitive oxide materials for high-rate
610 electrochemical energy storage, Energy Environ. Sci. 7 (2014) 1597–1614.
611 https://doi.org/10.1039/c3ee44164d.

612 [17] R. Ye, Z. Peng, T. Wang, Y. Xu, J. Zhang, Y. Li, L.G. Nilewski, J. Lin, J.M. Tour, In
613 Situ Formation of Metal Oxide Nanocrystals Embedded in Laser-Induced Graphene,
614 ACS Nano. 9 (2015) 9244–9251. https://doi.org/10.1021/acsnano.5b04138.

615 [18] L. Li, J. Zhang, Z. Peng, Y. Li, C. Gao, Y. Ji, R. Ye, N.D. Kim, Q. Zhong, Y. Yang, H.
616 Fei, G. Ruan, J.M. Tour, High-Performance Pseudocapacitive Microsupercapacitors
617 from Laser-Induced Graphene, Adv. Mater. 28 (2016) 838–845.
618 https://doi.org/10.1002/adma.201503333.

619 [19] P. Iamprasertkun, A. Krittayavathananon, A. Seubsai, Charge storage mechanisms of
620 manganese oxide nanosheets and N-doped reduced graphene oxide aerogel for high-
621 performance asymmetric supercapacitors, Nat. Publ. Gr. (2016) 1–12.
622 https://doi.org/10.1038/srep37560.

623 [20] P. Zhao, W. Li, G. Wang, B. Yu, X. Li, J. Bai, Z. Ren, Facile hydrothermal fabrication
624 of nitrogen-doped graphene/Fe2O3 composites as high performance electrode
625 materials for supercapacitor, J. Alloys Compd. 604 (2014) 87–93.
626 https://doi.org/10.1016/j.jallcom.2014.03.106.

627 [21] L. Lai, R. Li, S. Su, L. Zhang, Y. Cui, N. Guo, W. Shi, Controllable synthesis of
628 reduced graphene oxide / nickel hydroxide composites with different morphologies for
629 high performance supercapacitors, J. Alloys Compd. 820 (2020) 153120.
630 https://doi.org/10.1016/j.jallcom.2019.153120.

631 [22] L. Jiang, Z. Ren, S. Chen, Q. Zhang, X. Lu, H. Zhang, G. Wan, Bio-derived three-
632 dimensional hierarchical carbon-graphene-TiO2 as electrode for supercapacitors, Sci.
633 Rep. 8 (2018) 1–9. https://doi.org/10.1038/s41598-018-22742-7.

634 [23] Y.L. Zhang, L. Guo, H. Xia, Q.D. Chen, J. Feng, H.B. Sun, Photoreduction of
635 Graphene Oxides: Methods, Properties, and Applications, Adv. Opt. Mater. 2 (2014)
636 10–28. https://doi.org/10.1002/adom.201300317.

637 [24] R. Trusovas, G. Račiukaitis, G. Niaura, J. Barkauskas, G. Valušis, R. Pauliukaite,
638 Recent Advances in Laser Utilization in the Chemical Modification of Graphene

639 Oxide and Its Applications, Adv. Opt. Mater. 4 (2016) 37–65.
640 https://doi.org/10.1002/adom.201500469.

641 [25] N. Kurra, Q. Jiang, P. Nayak, H.N. Alshareef, Laser-derived graphene: A three-
642 dimensional printed graphene electrode and its emerging applications, Nano Today. 24
643 (2019) 81–102. https://doi.org/10.1016/j.nantod.2018.12.003.

644 [26] A. Longo, R. Verucchi, L. Aversa, R. Tatti, A. Ambrosio, E. Orabona, U. Coscia, G.
645 Carotenuto, P. Maddalena, Graphene oxide prepared by graphene nanoplatelets and
646 reduced by laser treatment, Nanotechnology. 28 (2017) 224002.
647 https://doi.org/10.1088/1361-6528/aa6c3c.

648 [27] M.F. El-Kady, R.B. Kaner, Scalable fabrication of high-power graphene micro-
649 supercapacitors for flexible and on-chip energy storage, Nat. Commun. 4 (2013) 1475–
650 1479. https://doi.org/10.1038/ncomms2446.

651 [28] W. Gao, N. Singh, L. Song, Z. Liu, A.L.M. Reddy, L. Ci, R. Vajtai, Q. Zhang, B. Wei,
652 P.M. Ajayan, Direct laser writing of micro-supercapacitors on hydrated graphite oxide
653 films, Nat. Nanotechnol. 6 (2011) 496–500. https://doi.org/10.1038/nnano.2011.110.

654 [29] Y. Zhang, L. Guo, S. Wei, Y. He, H. Xia, Q. Chen, H.B. Sun, F.S. Xiao, Direct
655 imprinting of microcircuits on graphene oxides film by femtosecond laser reduction,
656 Nano Today. 5 (2010) 15–20. https://doi.org/10.1016/j.nantod.2009.12.009.

657 [30] R. Ye, D.K. James, J.M. Tour, Laser-Induced Graphene: From Discovery to
658 Translation, Adv. Mater. 31 (2019) 1–15. https://doi.org/10.1002/adma.201803621.

659 [31] A. Lamberti, M. Serrapede, G. Ferraro, M. Fontana, F. Perrucci, S. Bianco, A.
660 Chiolerio, S. Bocchini, All-SPEEK flexible supercapacitor exploiting laser-induced
661 graphenization, 2D Mater. 4 (2017) 035012. https://doi.org/10.1088/2053-
662 1583/aa790e.

663 [32] P. Nayak, N. Kurra, C. Xia, H.N. Alshareef, Highly Efficient Laser Scribed Graphene
664 Electrodes for On-Chip Electrochemical Sensing Applications, Adv. Electron. Mater. 2
665 (2016) 1–11. https://doi.org/10.1002/aelm.201600185.

666 [33] Z. Peng, J. Lin, R. Ye, E.L.G. Samuel, J.M. Tour, Flexible and stackable laser-induced
667 graphene supercapacitors, ACS Appl. Mater. Interfaces. 7 (2015) 3414–3419.
668 https://doi.org/10.1021/am509065d.

669 [34] J. Lin, Z. Peng, Y. Liu, F. Ruiz-Zepeda, R. Ye, E.L.G. Samuel, M.J. Yacaman, B.I.
670 Yakobson, J.M. Tour, Laser-induced porous graphene films from commercial
671 polymers, Nat. Commun. 5 (2014) 1–8. https://doi.org/10.1038/ncomms6714.

672 [35] Z. Wan, S. Wang, B. Haylock, J. Kaur, P. Tanner, D. Thiel, R. Sang, I.S. Cole, X. Li,
673 M. Lobino, Q. Li, Tuning the sub-processes in laser reduction of graphene oxide by
674 adjusting the power and scanning speed of laser, Carbon N. Y. 141 (2019) 83–91.
675 https://doi.org/10.1016/j.carbon.2018.09.030.

676 [36] F. Cai, C.A. Tao, Y. Li, W. Yin, X. Wang, J. Wang, Effects of amount of graphene
677 oxide and the times of LightScribe on the performance of all-solid-state flexible
678 graphene-based micro-supercapacitors, Mater. Res. Express. 4 (2017) 036304.

https://doi.org/10.1088/2053-1591/aa65fb.

[37] M.F. El-Kady, V. Strong, S. Dubin, R.B. Kaner, Laser scribing of high-performance and flexible graphene-based electrochemical capacitors, Science (80-.). 335 (2012) 1326–1330. https://doi.org/10.1126/science.1216744.

[38] F. Clerici, M. Fontana, S. Bianco, M. Serrapede, F. Perrucci, S. Ferrero, E. Tresso, A. Lamberti, In situ MoS2 Decoration of Laser-Induced Graphene as Flexible Supercapacitor Electrodes, ACS Appl. Mater. Interfaces. 8 (2016) 10459–10465. https://doi.org/10.1021/acsami.6b00808.

[39] S. Wang, Z.S. Wu, S. Zheng, F. Zhou, C. Sun, H.M. Cheng, X. Bao, Scalable Fabrication of Photochemically Reduced Graphene-Based Monolithic Micro-Supercapacitors with Superior Energy and Power Densities, ACS Nano. 11 (2017) 4283–4291. https://doi.org/10.1021/acsnano.7b01390.

[40] V.H. Pham, T.D. Nguyen-Phan, X. Tong, B. Rajagopalan, J.S. Chung, J.H. Dickerson, Hydrogenated TiO2@reduced graphene oxide sandwich-like nanosheets for high voltage supercapacitor applications, Carbon N. Y. 126 (2018) 135–144. https://doi.org/10.1016/j.carbon.2017.10.026.

[41] L.L. Jiang, X. Lu, C.M. Xie, G.J. Wan, H.P. Zhang, T. Youhong, Flexible, free-standing TiO2-graphene-polypyrrole composite films as electrodes for supercapacitors, J. Phys. Chem. C. 119 (2015) 3903–3910. https://doi.org/10.1021/jp511022z.

[42] J. Kim, W.H. Khoh, B.H. Wee, J.D. Hong, Fabrication of flexible reduced graphene oxide-TiO2 freestanding films for supercapacitor application, RSC Adv. 5 (2015) 9904–9911. https://doi.org/10.1039/c4ra12980f.

[43] A. Ramadoss, S.J. Kim, Improved activity of a graphene-TiO2 hybrid electrode in an electrochemical supercapacitor, Carbon N. Y. 63 (2013) 434–445. https://doi.org/10.1016/j.carbon.2013.07.006.

[44] G. Sahoo, S.R. Polaki, N.G. Krishna, M. Kamruddin, Electrochemical capacitor performance of TiO2 decorated vertical graphene nanosheets electrode, J. Phys. D. Appl. Phys. 52 (2019). https://doi.org/10.1088/1361-6463/ab2ac5.

[45] W.S. Hummers, R.E. Offeman, Preparation of Graphitic Oxide, J. Am. Chem. Soc. 80 (1958) 1339. https://doi.org/10.1021/ja01539a017.

[46] Standard Graphene website, (n.d.). https://standardgraphene.com/product/go-v5010g/ (accessed 30 October 2020).

[47] V. Strong, S. Dubin, M.F. El-Kady, A. Lech, Y. Wang, B.H. Weiller, R.B. Kaner, Patterning and electronic tuning of laser scribed graphene for flexible all-carbon devices, ACS Nano. 6 (2012) 1395–1403. https://doi.org/10.1021/nn204200w.

[48] JEMS software, (n.d.). https://www.jems-swiss.ch/ (accessed 30 December 2020).

[49] J. Verbeeck, G. Bertoni, Deconvolution of core electron energy loss spectra, Ultramicroscopy. 109 (2009) 1343–1352. https://doi.org/10.1016/j.ultramic.2009.06.010.

718 [50] P. Simon, Y. Gogotsi, B. Dunn, Where do Batteries End and Supercapacitors Begin ?,
719 Science (80-.). 343 (2014) 1210–1211. https://doi.org/10.1126/science.1249625.

720 [51] A.J. Bard, L.R. Faulkner, Electrochemical Methods Fundamentals and Applications,
721 John Wiley & Sons, New York, USA, 2001.

722 [52] F. Béguin, V. Presser, A. Balducci, E. Frackowiak, Carbons and electrolytes for
723 advanced supercapacitors, Adv. Mater. 26 (2014) 2219–2251.
724 https://doi.org/10.1002/adma.201304137.

725 [53] D.R. Lobato-Peralta, D.E. Pacheco-Catalán, P.E. Altuzar-Coello, F. Béguin, A. Ayala-
726 Cortés, H.I. Villafán-Vidales, C.A. Arancibia-Bulnes, A.K. Cuentas-Gallegos,
727 Sustainable production of self-activated bio-derived carbons through solar pyrolysis
728 for their use in supercapacitors, J. Anal. Appl. Pyrolysis. 150 (2020).
729 https://doi.org/10.1016/j.jaap.2020.104901.

730 [54] V.A. Smirnov, A.A. Arbuzov, Y.M. Shul'ga, S.A. Baskakov, V.M. Martynenko, V.E.
731 Muradyan, E.I. Kresova, Photoreduction of graphite oxide, High Energy Chem. 45
732 (2011) 57–61. https://doi.org/10.1134/S0018143911010176.

733 [55] M. Gaboardi, A. Bliersbach, G. Bertoni, M. Aramini, G. Vlahopoulou, D. Pontiroli, P.
734 Mauron, G. Magnani, G. Salviati, A. Züttel, M. Riccò, Decoration of graphene with
735 nickel nanoparticles: Study of the interaction with hydrogen, J. Mater. Chem. A. 2
736 (2014) 1039–1046. https://doi.org/10.1039/c3ta14127f.

737 [56] G. Bertoni, E. Beyers, J. Verbeeck, M. Mertens, P. Cool, E.F. Vansant, G. Van
738 Tendeloo, Quantification of crystalline and amorphous content in porous TiO2
739 samples from electron energy loss spectroscopy, Ultramicroscopy. 106 (2006) 630–
740 635. https://doi.org/10.1016/j.ultramic.2006.03.006.

741 [57] D. Bersani, P.P. Lottici, X.Z. Ding, Phonon confinement effects in the Raman
742 scattering by TiO2 nanocrystals, Appl. Phys. Lett. 72 (1998) 73–75.
743 https://doi.org/10.1063/1.120648.

744 [58] F. Tuinstra, J.L. Koenig, Raman Spectrum of Graphite, J. Chem. Phys. 53 (1970)
745 1126–1130. https://doi.org/10.1063/1.1674108.

746 [59] A.C. Ferrari, Raman spectroscopy of graphene and graphite: Disorder, electron-
747 phonon coupling, doping and nonadiabatic effects, Solid State Commun. 143 (2007)
748 47–57. https://doi.org/10.1016/j.ssc.2007.03.052.

749 [60] G. Greczynski, L. Hultman, X-ray photoelectron spectroscopy: Towards reliable
750 binding energy referencing, Prog. Mater. Sci. 107 (2020) 100591.
751 https://doi.org/10.1016/j.pmatsci.2019.100591.

752 [61] J.F. Moulder, W.F. Stickle, P.E. Sobol, K.D. Bomben, Handbook of X-ray
753 photoelectron spectroscopy: a reference book of standard spectra for identification and
754 interpretation of XPS data, Perkin-Elmer Corporation, Physical Electronics Division,
755 Eden Prairie, Minnesota, USA, 1992.

756 [62] E. Frackowiak, F. Béguin, Carbon materials for the electrochemical storage of energy
757 in capacitors, Carbon N. Y. 39 (2001) 937–950. https://doi.org/10.1016/S0008-

6223(00)00183-4.

[63] Y.J. Oh, J.J. Yoo, Y.I. Kim, J.K. Yoon, H.N. Yoon, J.H. Kim, S.B. Park, Oxygen functional groups and electrochemical capacitive behavior of incompletely reduced graphene oxides as a thin-film electrode of supercapacitor, Electrochim. Acta. 116 (2014) 118–128. https://doi.org/10.1016/j.electacta.2013.11.040.

[64] M. Toupin, T. Brousse, D. Bélanger, Charge storage mechanism of MnO2 electrode used in aqueous electrochemical capacitor, Chem. Mater. 16 (2004) 3184–3190. https://doi.org/10.1021/cm049649j.

[65] J.P. Zheng, T.R. Jow, A New Charge Storage Mechanism for Electrochemical Capacitors, J. Electrochem. Soc. 142 (1995) 60–62. https://doi.org/10.1149/1.2043984.

[66] Q. Chen, X. Li, X. Zang, Y. Cao, Y. He, P. Li, K. Wang, J. Wei, D. Wu, H. Zhu, Effect of different gel electrolytes on graphene-based solid-state supercapacitors, RSC Adv. 4 (2014) 36253–36256. https://doi.org/10.1039/c4ra05553e.

[67] J.C. Pramudita, A. Rawal, M. Choucair, D. Pontiroli, G. Magnani, M. Gaboardi, M. Riccò, N. Sharma, Mechanisms of sodium insertion/extraction on the surface of defective graphenes, ACS Appl. Mater. Interfaces. 9 (2017) 431–438. https://doi.org/10.1021/acsami.6b13104.

[68] C. Zhong, Y. Deng, W. Hu, D. Sun, X. Han, J. Qiao, J. Zhang, Electrolytes for electrochemical supercapacitors, 2016. https://doi.org/10.1201/b21497-3.